ORIGINAL ARTICLE

Y. Lawrence Yao · Hongqiang Chen · Wenwu Zhang

Time scale effects in laser material removal: a review

Abstract In laser material removal using a continuous wave or long-pulsed laser, the primary material removal mechanism melts with molten metal often ejected by an assisting oxygen jet. Interactions between heat transfer, oxygen diffusion, and gas dynamics have been studied. In laser machining using a Q-switched solid state laser with pulse width on the order of nanoseconds, the primary material removal mechanism is ablation, but substantial melting is still present if a metallic material is concerned. Two mechanisms, ablation and melting, are modeled together and the property discontinuity and boundary conditions at the liquid/vapor interface are provided. When the laser pulse width further reduces to the order of picoseconds or femtoseconds, as in a Ti:sapphire laser, the dominant material removal mechanism changes yet again, with little thermal damage and wavelength independence observed. Thermal aspects are examined in the context of the short timescales of these pulses compared with the timescale of photon-electron-lattice interactions. Research needs in laser material removal in each of the three time regimes are discussed.

Nomenclature

A	surface absorptivity
b	Kerf width
b'	Laser beam radius
B	Constant in Eq. 17
c	Wave velocity
c_f	Friction factor
c_p	Heat capacity
c_{pe}	Heat capacity of electron

Y.L. Yao · H. Chenw
Department of Mechanical Engineering,
Columbia University,
New York, NY, USA

W. Zhang
GE Global Research Center,
Niskayuna, NY, USA

c_{pl}	Heat capacity of lattice
c_r	Traveling speed of the wave
C	Oxygen concentration
C'	Plasma correction coefficient
D, K	Diffusion coefficient and heat conductivity
f	Wave frequency
F_a	Absorbed laser fluence
F_{th}	Threshold laser fluence for evaporation with femtosecond pulses.
G_{eo}	Coupling coefficients for electron-optical phonon
G_{ol}	Coupling coefficients for optical phonon-acoustic phonon
h	Thickness of the liquid film
h'	Sensible heat
H	Enthalpy of the material
ΔH	Latent heat
I	Laser intensity
k_w	Wave number
k_B	Boltzmann constant
k_c	Heat conductivity
k_e	Electron thermal conductivity
k_l	Lattice thermal conductivity
l_d	Heat diffusion layer
l_s	Optical skin depth
L	Ablation depth pre pulse
L_m	Latent heat for melting
L_v	Latent heat of vaporization
M_v	Molecular mass
Ma_v	Vapor Mach number
N	Energy carrier number density
n	Electron density
p_o	Oxygen pressure
P_r, S_i	Normal and tangential stress parameters
Q	Heat flux
R	Universal gas constant
Rl	Reflectivity
s	Oxide layer thickness
s_m	Maximum thickness of the oxide layer
T_e	Electron cooling time

T_i	Lattice heating time
T_l	Duration of laser pulse
T	Temperature
$T_{electron}$	Electron temperature
$T_{lattice}$	Lattice temperature
T_0	Activation temperature for the diffusion.
t	Time
t_p	Inverse of frequency
U	Gas velocity profile
U_g	Streamwise gas velocity
U_e	Electron energy
U_o	Optical photon energy
U_l	Acoustic photon energy
ρ_g	Density of the gas
v	Kinetic viscosity of the melt
v_g	Kinetic viscosity of the gas
v	Velocity
v_f	Friction velocity
V	Interface velocity
w	Internal energy
W	Activation energy
x, y	Two-dimensional coordinates for the liquid film
x'	Distances along axial and radial directions
z	Direction perpendicular to the target surface
α	Dimensionless wave number
α'	Heat diffusivity
ρ	Density
β	Absorption coefficient of the material
β_a	Avalanche rate
β_t	Two-photon absorption coefficient
θ	Free carrier absorption coefficient
γ_s	Surface tension
γ_h	Specific heat ratio
γ_{el}	Parameter characterizing the electron-lattice coupling
τ	Mean shear stress
ζ, ξ	Defined in Eqs. 7 and 8
δ	Initial disturbance
μ	Viscosity of the melt
τ_e	Electron relaxation time
$\tau_{lattice}$	Time for energy transfer from electron to lattice
Ω	Specific heat of evaporation

Subscripts

o	Interface of oxide and oxygen
s	Interface of metal and oxide
v	Vapor phase
l	Liquid phase
i	Melt-vapor interface
vi	Vapor adjacent to the Knudsen layer
li	Liquid adjacent to the Knudsen layer

1 Introduction

Laser machining is accomplished by laser material interaction, and includes laser drilling, laser cutting and laser grooving, marking and scribing. A significant amount of research has been done for laser machining involving lasers operating in very different temporal modes, ranging from continuous wave (CW) to nanosecond pulses, and to femtosecond pulses [1–3].

The physical process in laser material interaction is important to the understanding of the capabilities and limitations of laser machining processes. When a laser beam impinges on the material, laser energy is first absorbed by free electrons. The absorbed energy then propagates through the electron subsystem and is transferred to the lattice as illustrated in Fig. 1 [4]. Three characteristic time scales are: T_e – the electron cooling time, which is on the order of 1 ps; T_i – the lattice heating time; and T_l – the duration of laser pulse. T_e and T_i are proportional to their heat capacity divided by the same constant, and the heat capacity of electron is much less than that of lattice; therefore, $T_e \ll T_i$. Three cases occur when T_l is in different ranges.

Case one: $T_l > 1$ ms $\gg T_i \gg T_e$, where T_l is of millisecond or infinite (continuous wave laser). The typical time scale is much larger than the electron-lattice energy coupling time, and the primary material removal mechanism melts with molten metal ejected by an assisting gas jet if metal is the target material. Classical heat transfer laws are fully appropriate in modeling these machining processes. Laser cutting is the most common process in this time region and used for steel, nonferrous metals, and nonmetals. The typical laser system in this time scale is a 10.6 micron CO_2 laser, which has power of a few KW and intensity of $1 \sim 2$ WM/cm^2.

Case two: $T_l > 1$ ns $\gg T_i \gg T_e$, where T_l is of nanosecond scale. In this case, electron absorbed laser energy has enough time to be transferred to the lattice, electron and the lattice can reach thermal equilibrium, and the main energy loss is the heat conduction into the solid target. Material is first melted, and when the beam is strong enough, evaporation occurs from the liquid state. Laser drilling, grooving, marking, or scribing are typical processes in this regime, where slight melting is followed by quick evaporation. Also the heat affected zone (HAZ) is usually smaller than that of the CW laser processing. However, the existence of a melting layer makes precise material removal dif-
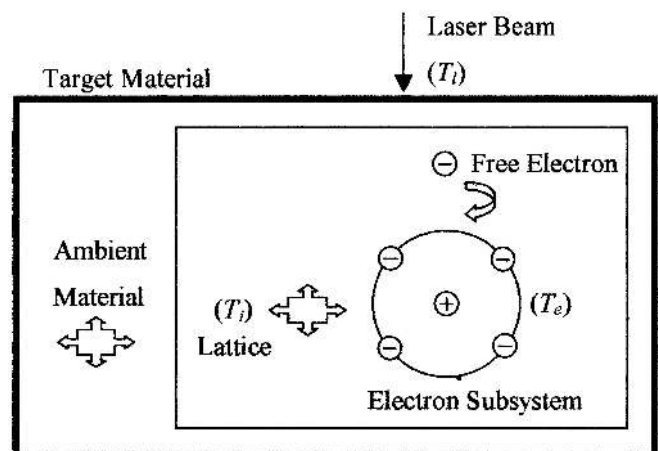

Fig. 1. Energy flow in laser-material interaction [4]

ficult. In this time scale, the typical laser used is the Q-switched solid state laser, such as a Nd:YAG laser, which has tripled frequency (355 nm), and with intensity of $100 \sim 200 \, \mathrm{J/cm^2}$. The materials used are often nonferrous metals such as Cu and Al and alloys because of their good absorptivity at the UV wavelength.

Case three: $T_l \ll T_e \ll T_i$, where T_l is of femtosecond scale, and laser pulse duration is shorter than the electron cooling time. Electrons are heated instantly, then, in about 1 ps, electrons transfer their energy to their positive lattice ions. When this energy intensity is high enough, which is often true for ultrafast pulsed lasers, those ions get energy high enough to break the bonding of the lattice structure. They break off instantly without having time to transfer their energy to their neighboring lattice ions; thus, direct solid-vapor transition occurs. Heat conduction into the target can be neglected; the heat affected zone is greatly reduced. For melting-free ablation to be possible, two conditions must be met: ultrashort pulse duration and high enough pulse energy. Since direct solid-vapor transition can be achieved so that all processes such as cutting, drilling, grooving, marking, or scribing can be used in this time region, and precise material removal is possible. In this time scale, the typical laser used is Ti:sapphire laser with wavelength 780 nm and intensity from $0.1-10 \, \mathrm{J/cm^2}$. Almost all materials such as metals, alloys, polymers, and ceramics can be removed at this time scale, and the absorptivity is wavelength independent.

Thus, the thermal aspects such as internal thermal transport, melting, vaporization, thermodynamic phase equilibrium, and electron-lattice energy coupling in laser material processing need to be modeled quite differently under different cases, which will ultimately affect subsequent process outcomes. In this paper, thermal problems existing in different time regimes of laser material removal are discussed, key relationships are highlighted, typical examples are given, selected results are discussed, and further work is discussed.

2 Continuous wave laser cutting

For laser cutting using a continuous wave laser, the typical time scale is much larger than the electron-lattice energy coupling time, and the primary material removal mechanism melts with molten metal ejected by an assisting gas jet. Classical heat and mass transfer laws are fully appropriate when applied to modeling those machining processes [1], and it is generally the view that thermal problems in this time regime have been well understood and solved. In the majority of industrial practice, however,

laser cutting of steel (sometimes including stainless steel) uses oxygen as an assisting gas to provide exothermic energy, and to help increase cutting speed. One important phenomenon in oxygen-assisted cutting is the formation of striation [5]. The explanations given for this phenomenon have been internal instability of the cutting process [6], and cyclic oxidation [7], which is shown as Fig. 2. It is explained that, for diffusion controlled reactions, the rate of a chemical reaction is time dependent, being rapid in the early stages, but decreasing markedly as the thickness of the oxide layer increases. So, the oxide layer will expand rapidly at first but slow down afterwards. Once the oxide is blown out from the cutting front, due to a sudden decrease of the oxide layer, another expansion will begin.

Although [7] gives a quite convincing explanation on the expansion of the oxide layer, it does not clearly explain how the oxide layer is suddenly reduced. Moreover, the explanation is empirically based, and when quantitative analysis is needed, the heat transfer and energy balance will become more complex in modeling the cutting process when the oxygen diffusion and oxidation process are taken into account. A theory of the unstable characteristic of the melt ejection combined with the oxidation oscillation is proposed to explain the mechanism of the striation generation [8]. A schematic of laser cutting of mild steel is shown in Fig. 3.

2.1 Physical mechanism of melt removal and striation formation

Consider the top part of the molten front in Fig. 4. At low cutting speeds, the liquid film has a relatively long exposure time in
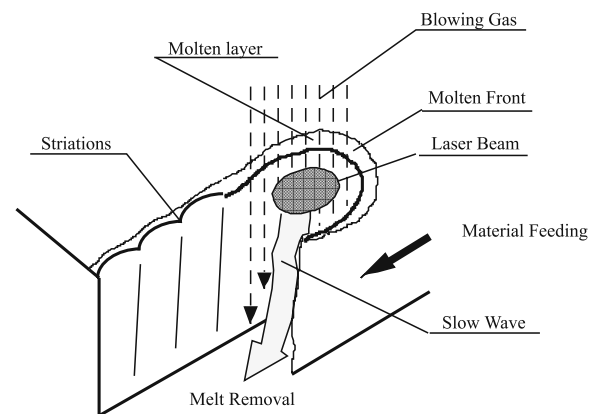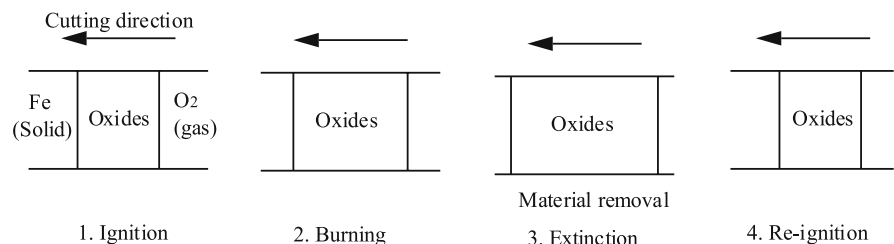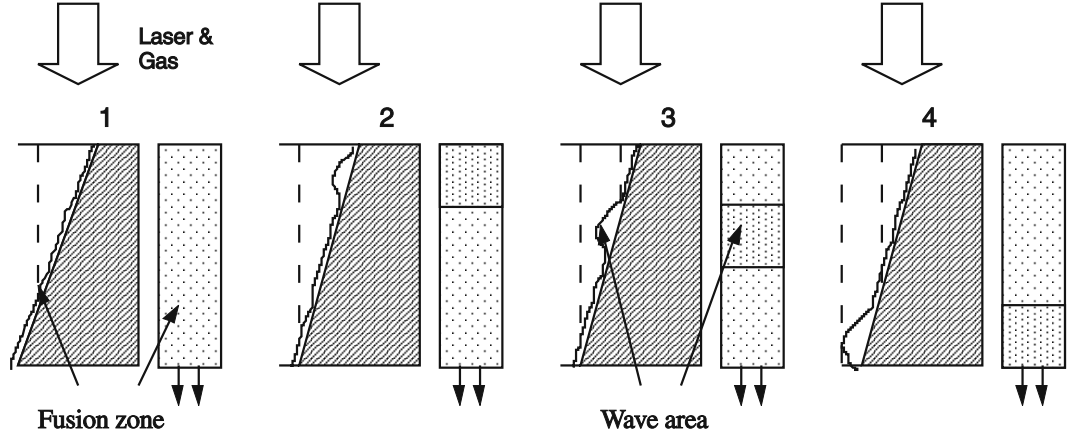
Fig. 3. Schematic of oxygen cutting of mild steel [8]

Fig. 2. The oxidation model proposed by Ivarson et al. [7]

Fig. 4. Schematic of the molten front change at high cutting speeds [8]

the gas flow, and the liquid film will usually rupture since there is not enough liquid flow rate on the top part of the molten front. This phenomenon has been observed and described by [5]. When the cutting speed increases, the period of film rupture becomes shorter. At some critical cutting speeds, there is not enough time for instabilities to develop causing film rupture, and there is always a liquid film on the top of the molten front. This was described by [5] as "steady cutting", which corresponds to a cutting speed above 2 m/min. This thin liquid film for mild steel of a certain thickness, however, may still be unstable and instead of film rupture, slow waves may be generated (it is shown later that the thickness of the liquid film is below the critical thickness under which slow waves are generated). Once the crest of the slow wave moves downwards from the top of the molten front, much more melt is removed and oxidation, coupled with heat conduction, begins to expand. The process is fast at first and slows down until another wave crest comes and moves the melt downwards. Thus an expansion-compression cyclic pattern is still formed above the so-called critical cutting speed.

2.2 Quantitative prediction of striation depth and frequency

2.2.1 Prediction of striation frequency

The analysis of the instabilities generated on a liquid film by an adjacent high speed gas jet begins with the linearized Navier-Stokes equations of the liquid film. Only two-dimensional harmonic disturbances are considered here. For neutrally stable disturbances, the analysis gives the results of:

$$P_r + \frac{3S_i}{2kh} = \gamma_s k^2 h \ , and \tag{1}$$

$$c_r = v_{interface} \ , \tag{2}$$

where h is the thickness of the liquid film, $v_{interface}$ is the interface velocity, k is the wave number, γ_s is the surface tension. P_r and S_i are stress parameters such that

$$\sigma_{yy} = P_r \eta \tag{3}$$

$$\sigma_{xy} = S_i \eta \ . \tag{4}$$

The sinusoidal disturbance η has the form of

$$\eta = \delta e^{ik(x-ct)} \ , \tag{5}$$

where δ is the initial disturbance of a small value, t is the time, k is the wave number, c is the wave velocity, which may be complex, and x and y are two-dimensional coordinates for the liquid film.

In the aforementioned physical model, the striation frequency is equivalent to the oscillation frequency of melt ejection and oxidation. Under high speed cutting conditions, the frequency should be equivalent to the slow wave frequency. The wave number of the slow wave is approximately taken as the critical wave number at which the mean shear stress τ attains the minimum value. Undamped disturbances for the liquid film of thickness h are sustained at such a minimum value. Substituted by the proper stress evaluation, Eq. 1 becomes

$$\frac{\varsigma}{c_f} \left[\frac{k\tau}{\rho} + \frac{3\xi v^{2/3}}{2h} \left(\frac{k\tau}{\rho} \right)^{2/3} \right] = \frac{\gamma k^2}{\rho} \ , \tag{6}$$

where c_f is the friction factor, and ρ is the density of the melt. The expressions for ζ and ξ are:

$$\varsigma = \int_0^\infty \left(U(y)/U_g \right) e^{-\alpha y} d(\alpha y) \ , and \tag{7}$$

$$\xi = 1.188 \left(\frac{v_g}{v} \right)^{2/3} \left(\frac{\rho_g}{\rho} \right) \ , \tag{8}$$

where $\alpha = kh$ is the dimensionless wave number, $U(y)$ are gas velocity profiles, which are assumed to follow the 1/7th power law [9], U_g is the streamwise gas velocity, v_g and v are kinetic viscosity of the gas and the melt ,respectively, and ρ_g is the gas density.

Taking the derivative $\partial\tau/\partial k$ of Eq. 6, one obtains the positive critical wave number:

$$k = \frac{I\tau}{4c_f\gamma} \ . \tag{9}$$

The mean stress is evaluated according to:

$$\tau = \mu \frac{v_{interface}}{h} , \tag{10}$$

where μ is the viscosity of the melt. The interfacial velocity can be calculated using the 1/7th power law of the mean velocity profile [9], that is,

$$\frac{U_g}{v_*} = 8.74 \left(\frac{b v_*}{2 v_g}\right)^{1/7} \tag{11}$$

$$\rho_g v_*^2 = \frac{\mu v_{interface}}{h} , \tag{12}$$

where b is the kerf width, and v_f is the friction velocity. The properties of the gas phase should be taken at the local temperature.

Theoretical result shows that the wave speed is equal to the interfacial velocity (Eq. 2). However, the experimental measurements show that the wave speed is actually less than the interfacial velocity. A reasonable approximation is obtained by considering a coefficient of, say, 0.8 [10]:

$$c = 0.8 v_{interface} , \tag{13}$$

where c is the wave velocity and v the interfacial velocity. This takes into account the nonlinear effects which may reduce the wave velocity. Thus, we can use v calculated from Eqs. 11 and 12 to approximate wave velocity. The wave frequency is then,

$$f = 0.8 v_{interface} k / 2\pi . \tag{14}$$

2.2.2 Prediction of striation depth

As mentioned before, striation formation has been found to be strongly related to oxidation in laser cutting. The exothermic oxidation typically contributes nearly half of the total energy input. The heat conduction and oxidation take the same parabolic forms as:

$$\frac{\partial C}{\partial t} + U(y)\frac{\partial C}{\partial x} = \frac{\partial}{\partial y}\left(D\frac{\partial C}{\partial y}\right) , and \tag{15}$$

$$\rho\frac{\partial c_p T}{\partial t} + \rho U(y)\frac{\partial c_p T}{\partial x} = \frac{\partial}{\partial y}\left(K\frac{\partial T}{\partial y}\right) , \tag{16}$$

where C is the oxygen concentration, ρ the density, c_p the heat capacity, and D and K are diffusion coefficient and heat conductivity.

If the quasi steady state approximation that the concentration on the oxide surface is independent of the oxide film is valid, the diffusion controlled oxidation process can be described as:

$$\frac{ds}{dt} = BD\frac{(C_o - C_s)}{s(t)} \approx BD\frac{C_o}{s(t)} , \tag{17}$$

where s is the oxide layer thickness, subscript s denotes the metal-oxide interface and o the oxide-oxygen interface, C_s is near zero because of consumption of oxygen at the reaction

plane, and B is a constant. The temperature T dependence of the diffusion coefficient is due to an exponential factor containing an activation energy W and Boltzmann constant k_B:

$$D \propto \exp\left(-\frac{W}{k_B T}\right) . \tag{18}$$

Note that C_o is also temperature dependent (T):

$$C_o \propto \exp\left(-\frac{w}{k_B T}\right) , \tag{19}$$

where w is the internal energy. The oxidation equation can be written as:

$$\frac{ds}{dt} = A\left(p_0\right)\frac{\exp\left(-T_0/T\right)}{s(t)} , \tag{20}$$

where A is a coefficient, which has presumably a linear relationship with the oxygen pressure p_o at the surface of the molten front. T_0 is the activation temperature for the diffusion. An estimate for s can be achieved by neglecting temperature variation and simply integrating Eq. 20 to give the well known parabolic equation:

$$s_m^2 = A\left(p_0\right)t_p , \tag{21}$$

where s_m is the maximum thickness of the oxide layer. The time period t_p is the inverse of frequency from Eq. 14. If one calculates the striation frequency from Eq. 14, the maximum depth of the striations can be estimated from Eq. 21 if the coefficient is experimentally calibrated.

2.3 Typical results and further work

The predicted striation wavelength and the experimental results are given in Fig. 5, and they are in agreement. The increase in cutting speed causes the liquid film thickness and thus causes the interfacial velocity to increase. As a result, the striation frequency increases, but not as much as the increase of the cutting
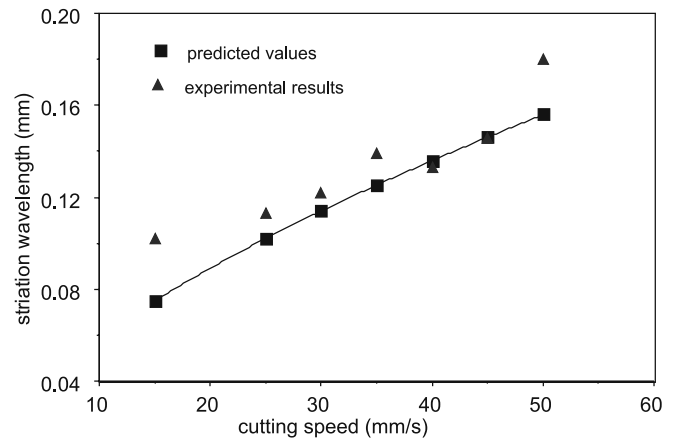

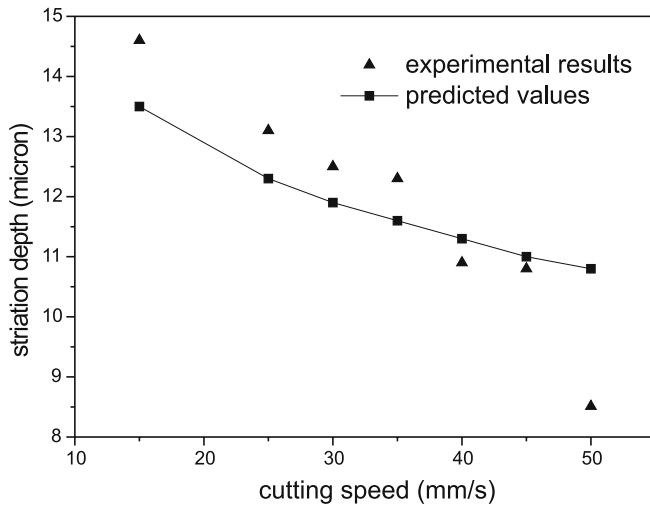**Fig. 5.** Striation wavelength versus cutting speed [8]

Fig. 6. Maximum striation depth versus cutting speed [8]

speed. The net result, therefore, is that the striation wavelength increases with the cutting speed.

Striation depth is evaluated using Eq. 21. This assumes that the parabolic growth of the oxide layer is directly related to the striation depth. Figure 6 shows the predicted maximum striation depth against the experimental measurements. The coefficient in Eq. 21 is calibrated to be a constant of 4×10^{-8}. The increase of the striation frequency with the cutting speed gives a shorter interaction period for the oxidation and the melting process; thus, reduces the striation depth. The prediction is consistent with the experimental results.

In the current prediction of striation wavelength, the physical properties of gas and liquid phases are assumed to be constant. The approximation is valid only when the energy balance does not change significantly as the cutting speed or the gas pressure varies. A more accurate model would incorporate the energy balance into the calculations. Also the calculation of heat transfer and oxidation will be extended to three-dimensional realistic cut geometry. The effect of vaporization and multiple reflections will be considered. The time-dependent calculation will take into account the time-dependent laser heat flux so that the calculation is applicable to pulsed laser machining.

3 Q-switched laser machining with pulse width on the order of nanoseconds

In laser machining using a Q-switched laser with pulse width on the order of nanoseconds, the primary material removal mechanism is ablation, but substantial melting is still present if a metallic material is concerned. The electron relaxation time τ_e for copper is 7×10^{-17} s. The time for energy transfer from electron to lattice $\tau_{lattice}$ is on the order of 10^{-12} s. So, for the 50 ns pulse duration time, which is about 50 000 times of $\tau_{lattice}$, the electron-gas temperature and the lattice temperature in the target material are about the same, and thermal equilibrium can be assumed. As a result, traditional heat transfer can be safely applied to laser machining using nanosecond pulses.

Many models of laser machining using nanosecond pulses have also been developed. Paek et al. [11] developed a theoretical model to predict the temperature profile assuming a laser beam of circular cross section and uniform intensity. Dabby et al. [12] calculated the transient temperature and penetrating velocity during the vaporization process. The models more recently developed [13] considered effects of gas dynamics and Knudsen layer discontinuity during the ablation process. These models assume one-dimensional heat transfer in target material, recognizing that the machining depth is much smaller than the diameter of the hole, which is reasonable for relatively large holes (a few hundred microns). Figure 7 shows the ablation depth and melting depth for different materials [13]. It is clear that the depth is much smaller compared to the laser spot size, which is 0.5 mm and the one-dimensional assumption is validated. As a result, however, the effects of beam profiles and cavity profiles are not considered. These factors are important when the size of the hole is comparable to the drilling depth. The significant challenge in the thermal aspect at this time scale is how to model ablation and melting together. Also proper boundary conditions and property discontinuity at the liquid/vapor interface and laser/plasma interaction are necessary to be considered. The model in this paper concentrates on heat transfer and associated phase changes inside the target material. Stefan and kinetic boundary conditions are applied at the liquid-vapor interface, and property discontinuity across the Knudsen layer is considered.

Fig. 7. a melting depth **b** ablation depth for Au, Cu, and Al substrates subjected to laser pulse of 26 ns duration and of different fluences; the ambient pressure is $P = 1$ atm and the laser spot radius is $r = 0.5$ mm [13]
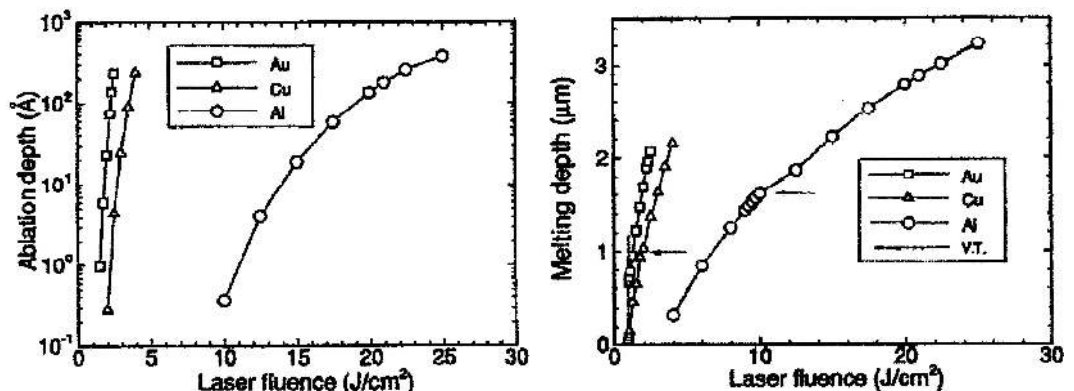
Heat conduction is calculated using the enthalpy method. Most importantly, the axisymmetric model allows considerations of laser beam distribution and its coupling with the target material, which is important when the ablation extent is in the same order as the ablation depth [14].

3.1 Modeling background

Under the irradiation of a laser beam, target material is first heated from room temperature to melting temperature, at which point melting takes place. Depending on laser intensity and material properties, the molten part of material will be evaporated by additional heating when it reaches the vaporization point and a vapor-filled cavity is formed (Fig. 8). A thin, so-called Knudsen layer exists at the melt-vapor interface, where the state variables undergo discontinuous changes across the layer [10]. When the incident laser intensity exceeds a certain threshold, vaporization leads to plasma formation, which will absorb a certain percentage of laser energy. The more the intensity goes beyond the threshold, the denser the plasma, and the more percentage of absorption. In practice, an assisting gas jet could disperse the plasma plume sideward and lower the plasma density, but the plasma effects still exist. By introducing a correction coefficient in the modeling of laser intensity, the plasma effects are corrected for. The motion of molten material caused by the Marangoni effect [15] is neglected.

The governing equation for energy balance can be written as:

$$\frac{\partial h'}{\partial t} + \frac{\partial \Delta H}{\partial t} = \frac{\partial}{\partial x'}\left(\alpha'\frac{\partial h}{\partial x'}\right) + \frac{1}{r}\frac{\partial}{\partial r}\left(r\alpha'\frac{\partial h'}{\partial r}\right) , \qquad (22)$$

where α' is heat diffusivity, ρ is density, and x' and r are distances along axial and radial directions, as shown in Fig. 8. The enthalpy of the material (the total heat content) can be expressed as $H = h' + \Delta H$, i.e., the sum of sensible heat, $h' = c_p T$
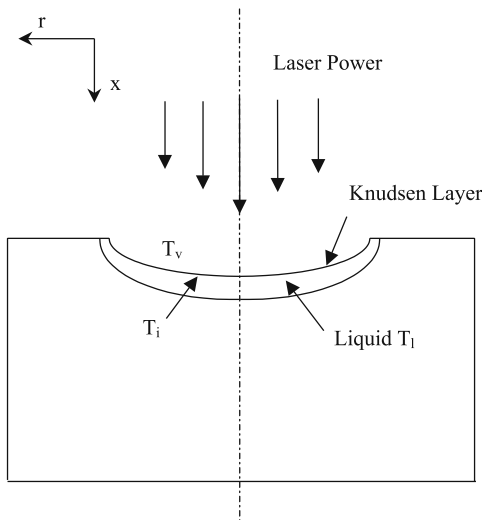

Fig. 8. Calculation domain [14]

$(c_p$ is the heat capacity, and T is the temperature), and latent heat ΔH. It either varies with L_m, the latent heat for melting, or is zero. The enthalpy formulation allows one to trace the melting boundary as functions of time without regeneration of calculation grids [16].

At the melt-vapor front, the Stefan boundary condition is applied,

$$Q + k\left(\frac{\partial T}{\partial x} + r\frac{\partial T}{\partial r}\right) + \rho_l v_i L_v - \rho_v v_v\left(c_p T_i + E_v\right) = 0 , \qquad (23)$$

$$E_v = \frac{RT_v}{(\gamma - 1)M_v} + \frac{1}{2}v_v^2 , \qquad (24)$$

$$Q = C(1 - Rl)I(t)e^{-\left(\frac{r}{b}\right)^2}e^{-\beta x} , \qquad (25)$$

where Q is the laser heat flux, which depends on reflectivity Rl, absorptivity β and the plasma correction coefficient C'. I is the laser intensity which is a function of time, and b' is the laser beam radius. The subscripts l, v and i denote liquid phase, vapor phase, and vapor-liquid interface, respectively. The gas energy E_v includes the internal energy and the kinetic energy. k_c is the heat conductivity, v the velocity, R the universal gas constant, γ_h the specific heat ratio, L_v the latent heat of vaporization, and M_v the molecular mass. The velocity, the laser energy flux, and the heat conduction flux are valued along the normal direction of the cavity profile. The vapor-liquid front is determined by tracing the temperature. As long as the temperature at certain grid points reaches vaporization temperature, the grids which have temperatures larger than vaporization temperature are taken out as the gas phase and the calculation starts from the newly determined vapor-liquid front.

The following analytic relationships [17] are applied to account for the discontinuity of the Knudsen layer:

$$\frac{T_{vi}}{T_{li}} = \left[\sqrt{1 + \pi\left(\frac{m}{2}\frac{\gamma - 1}{\gamma + 1}\right)^2} - \sqrt{\pi}\frac{m}{2}\frac{\gamma_h - 1}{\gamma_h + 1}\right]^2 \qquad (26)$$

$$\frac{\rho_{vi}}{\rho_{li}} = \sqrt{\frac{T_{li}}{T_{vi}}}\left[\left(m^2 + \frac{1}{2}\right)e^{m^2}erfc(m) - \frac{m}{\sqrt{\pi}}\right]$$
$$+ \frac{1}{2}\frac{T_{li}}{T_{vi}}\left[1 - \sqrt{\pi}me^{m^2}erfc(m)\right] \qquad (27)$$

$$e^{m^2}erfc(m) \approx 0.34802a - 0.09588a^2 + 0.74786a^3 \qquad (28)$$

$$a = 1/(1 + 0.47047m) , \quad m = \frac{v_{vi}}{\sqrt{2RT_{vi}/Ma_v}} , \qquad (29)$$

where subscript vi denotes the values of the vapor adjacent to the Knudsen layer, and li denotes the values of liquid adjacent to the Knudsen layer. Ma_v is the vapor Mach number, and $erfc(m)$ is the complementary error function.

The gas velocity is obtained from mass conservation:

$$\rho_l v_i = \rho_v\left(v_i + v_v\right) , \qquad (30)$$

where v_i is the velocity of the melt-vapor interface, and v_v is the vapor velocity.

The boundary conditions given by Eqs. 23–25 depend on the vapor temperature, which is back related to the vapor-liquid

interface temperature through Eqs. 26–29. Some thermal properties are treated as temperature sensitive. The calculation process is thus iterative between the gas, liquid, and solid phase until proper convergence is achieved. A control-volume based computation scheme was developed to solve the coupled governing equations. The two-dimensional discrete equations are written in the fully implicit form. The coefficients of variables are linearized between each time step to facilitate the convergence. The computational domain is taken large enough (5 times of beam radius in both x' and r directions) so that the temperatures at external boundaries can be considered as room temperature. The convective and radiative heat transfer on the top surface is negligible compared with conduction heat loss.

3.2 Typical results and further work

Figure 9 shows the simulation results of the cavity profile at the end of a 50-ns pulse at different levels of beam intensities. The material starts to melt at 4×10^7 W/cm^2 (Fig. 9a). The material starts to vaporize at 9.8×10^7 W/cm^2, and at 1.15×10^8 W/cm^2 a cavity on top is visible (Fig. 9c). In between pure melting evolves (Fig. 9b). The vertical lines denote the molten layer.

Figure 10 shows the temperature contours in the material after 50 ns for the intensity of 6×10^8 W/cm^2 and 1.5×10^9 W/cm^2. It is seen that the temperature quickly drops to room temperature about three times that of the beam radius away from the cavity center with larger gradient close to the cavity surface.

(a)

(b)

(c)
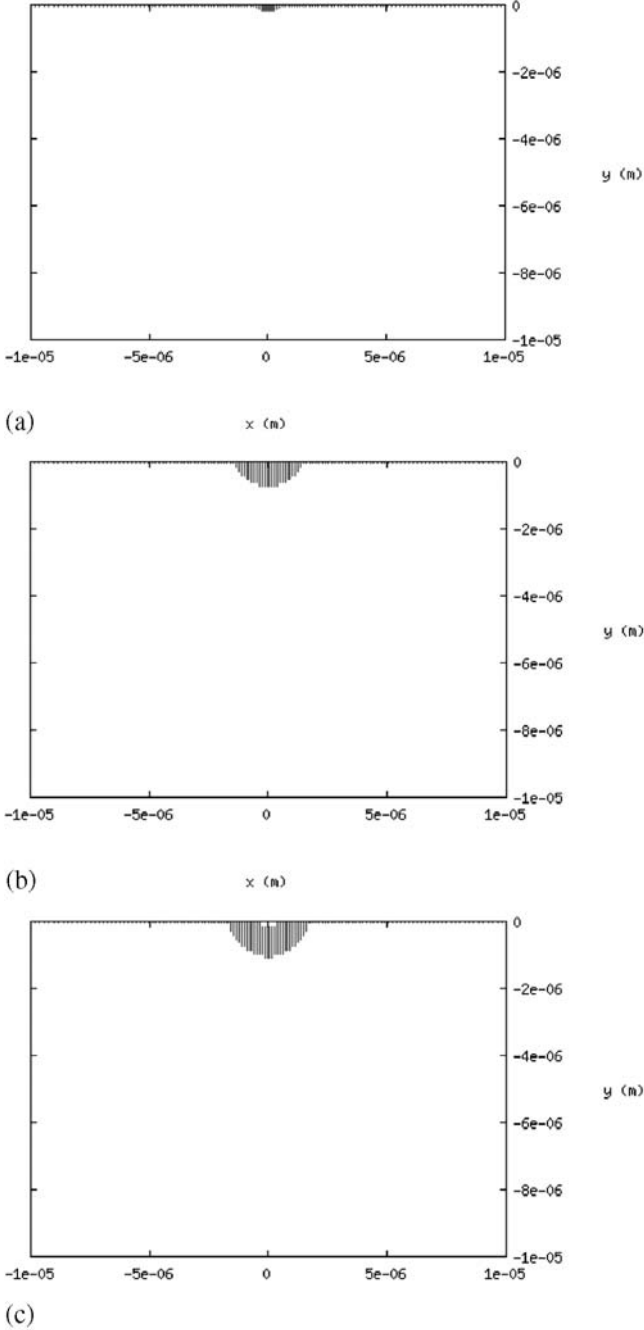
Fig. 9. Cavity profiles at the end of a 50 ns laser pulse under different laser intensity (wavelength $\lambda = 355$ nm, Gaussian beam, beams radius $b = 2.25\,\mu$m, Cu; vertical coordinates are in the x direction, and horizontal coordinates are in the r direction) [14]

(a)

(b)
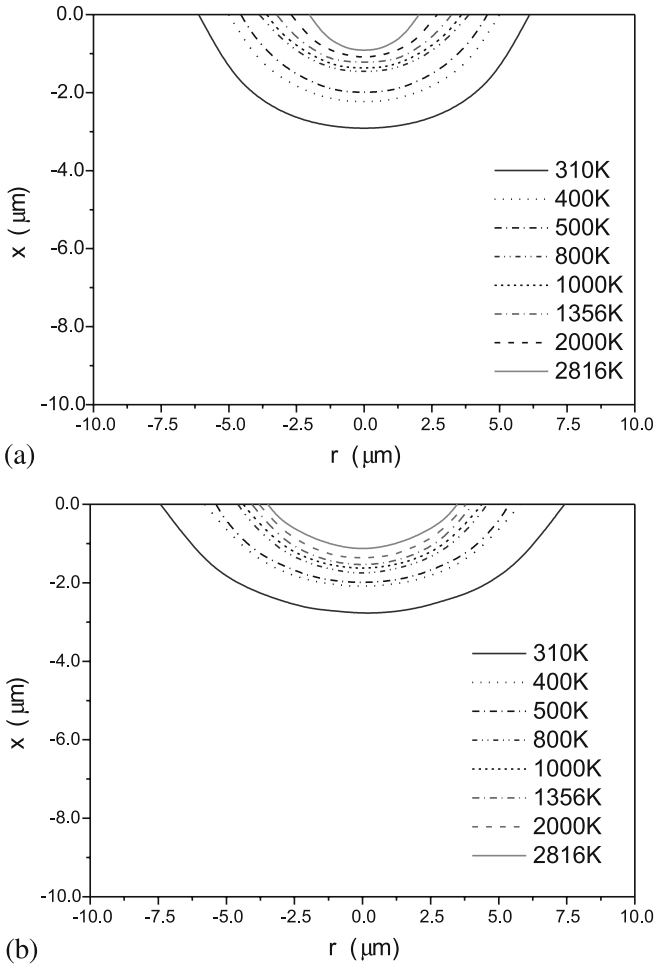
Fig. 10a,b. Temperature contours at the end of a 50 ns laser pulse **a** $I = 6 \times 10^8$ W/cm^2 **b** $I = 1.5 \times 10^9$ W/cm^2. (wavelength $\lambda = 355$ nm, Gaussian beam, beam radius $b = 2.25\,\mu$m, Cu) [14]

As mentioned before, by introducing a correction coefficient in the modeling of laser intensity, the plasma effects are corrected for. Actually, the dynamic evolution of plasma and nonlinear absorption are quite complex and the complete thermal interaction between plasma and melted material needs to be considered as a whole for more accurate modeling.

4 Ultrashort pulsed laser machining

4.1 Mechanism of ultrashort pulsed laser material removal

For ultrashort pulsed laser machining (10 ps or less), the material can be ablated precisely with little or no collateral damage, and wavelength independence is observed. When a laser beam interacts with a material, electrons are excited by the absorption of photons. The electrons are heated to high temperature by absorbing laser energy through collisions with ions. Subsequent electron-photon interactions allow the absorbed energy to be transferred to the lattice in a time frame of picoseconds for most materials. For femtosecond pulses, there is insufficient time for energy transfer to the lattice; consequently, thermal damage is minimal [18]. Because the extreme intensity of the light, along with its short time frame compared with classical heat transfer, the thermal problems are quite different in ultrashort laser machining due to the two following effects.

4.1.1 Thermal diffusion effect

The difference in short- and long-pulse laser processing of materials begins with the way the laser pulse energy is deposited in the target material. Initially, the laser energy is deposited in the optical skin depth $l_s = 1/\beta$, where β is the absorption coefficient of the material. During the laser irradiation, the deposited energy is also transferred out of this layer to a depth given by the heat diffusion layer $l_d = \sqrt{DT_l}$, where D is the heat diffusion coefficient, and is T_l the laser pulse width defined before. When the laser pulse width T_l is long so that $l_d > l_s$, laser processing is in the long-pulse regime. If the pulse width is so short such that $l_d < l_s$, the heat diffusion depth is limited to the very small skin depth. This is the regime of ultrashort-pulse laser processing. For ultrafast laser processing, the nonspread of the deposited laser energy causes rapid vaporization of the material. Laser drilling and cutting with ultrashort laser pulses are therefore through direct evaporative ablation.

4.1.2 Nonlinear absorption

This is the second factor that contributes to production of smaller interaction volumes. Multiphoton absorption and avalanche ionization are insignificant at low intensities, but become increasingly probable at the gigawatt- and terawatt-per-square-centimeter intensities, which these lasers create [18] partially because of the ultra short pulse width involved.

4.2 Modeling of the material removal process using an ultrashort laser

Modeling of the material removal process using ultrashort laser has been discussed by many researchers. A theoretical model is presented by [3] for laser ablation of solid targets by femtosecond Ti:Sapphire laser pulses. It assumes that the thermalization within the electron subsystem is very fast, and that the electron and the lattice subsystems can be characterized by their temperatures ($T_{electron}$ and $T_{lattice}$). The energy transport into the metal can be described by the following one-dimensional, two-temperature diffusion model:

$$c_{pe} \frac{\partial T_{electron}}{\partial t} = -\frac{\partial Q(z)}{\partial z} - \gamma_{el}(T_{electron} - T_{lattice}) + S \ , \tag{31}$$

$$c_{pl} \frac{\partial T_{lattice}}{\partial t} = \gamma_{el}(T_{electron} - T_{lattice}) \ , \tag{32}$$

$$Q(z) = -k_e \partial T_{electron}/\partial z \ , \quad S = I(t)A\beta \exp(-\beta z) \ . \tag{33}$$

For femtosecond pulses, the laser pulse duration is much shorter than the electron cooling time, $T_l \ll T_e$, which is equivalent to $c_{pe}T_{electron}/t \gg \gamma_{el}T_{electron}$. The electron-lattice coupling can be neglected. At the end of the laser pulse the electron temperature is given by:

$$T_{electron}(T_l) \cong \left(\frac{2F_a\beta}{c_{pe}}\right)^{1/2} \exp(-2z\beta) \ , \tag{34}$$

where $F_a = I \cdot T_l$ is the absorbed laser fluence. After the laser pulse, the electrons are rapidly cooled due to the energy transfer to the lattice and heat conduction into the bulk. The condition for strong evaporation is

$$F_a \geq F_{th} \exp(\beta z) \ , \tag{35}$$

where $F_{th} \cong \rho \Omega/\beta$ is the threshold laser fluence for evaporation with femtosecond pulses. Then the ablation depth per pulse L is

$$L \cong \beta^{-1} \ln(F_a/F_{th}) \ . \tag{36}$$

Due to the very short time scales involved in the ablation with femtosecond laser pulses, the ablation process can be considered as a direct solid-vapor transition. During all these processes, thermal conduction into the target can be neglected in a first approximation.

This model works well for the metals and may be sufficient for materials with a significant band gap [18]. However, this model assumes that reflectivity is constant and does not consider carefully the effect of nonlinear absorption on the ablation volume (multiphoton absorption and avalanche ionization). Feit et al. [19] suggested that for ultrashort laser pulses, first, laser intensities corresponding to breakdown produce electrons via photo ionization, and these electrons initiate the avalanche. This highly nonlinear process results in a very sharp ablation threshold so that material removal is highly localized and reproducible. Also, for very short pulses, laser energy is absorbed by the electrons much faster than it can be transferred to the lattice. Since the lattice does not heat appreciably during the pulse, there is no need

to track the flow of energy into the lattice to account for thermal and mechanical stresses. The growth of the conduction electron density n is then described approximately by the equation:

$$\frac{\partial n}{\partial t} = \beta_a n + S_m \ , \tag{37}$$

where S_m represents the multiphoton absorption source term. β_a is the avalanche rate, which is proportional to laser intensity I provided that the intensity is larger than a threshold value. For simplicity, it was assumed that I and S_m are independent of time. The general solution of the above equation is of the form:

$$n = \left(\frac{S_m}{\beta_a} + n_0\right) \exp\left(\beta_a t\right) - \frac{S_m}{\beta_a} \ , \tag{38}$$

where n_0 is the initial concentration. The avalanche rate β_a can be simply understood as the rate at which energy is used to generate new electrons.

Recently, [20] proposed a one-dimensional, three-temperature model. The energy transport is utilized to predict the carrier temperature and lattice temperature, as well as the electron and vapor flux emitted from the surface for femtosecond laser ablation on crystalline silicon. Nonlinear absorption and electron-lattice interaction are both considered. The gradient of the laser beam intensity is

$$\frac{dI}{dz} = -\beta I - \beta_t I^2 - \theta N I \ , \tag{39}$$

where β is the linear absorption coefficient, β_t is the two-photon absorption coefficient, and θ is the free carrier absorption coefficient.

The total energy balance equations for the electron and lattice systems using the relaxation time approximation can be written as follows:

$$\frac{\partial U_e}{\partial t} + \nabla \cdot \left(-k_e \nabla T_{electron}\right) = \left(1 - R_{refz}\right)\left(\beta_t + \theta N\right) I(x.t)$$
$$+ \left(1 - R_{refl}\right)^2 \beta_t^2 I^2(z, t)$$
$$- G_{eo}\left(T_{electron} - T_{photon}\right) \ , \tag{40}$$

$$\frac{\partial U_o}{\partial t} = G_{eo}\left(T_{electron} - T_{photon}\right) - G_{ol}\left(T_{photon} - T_{lattice}\right) \ , \tag{41}$$

$$\frac{\partial U_l}{\partial t} + \nabla \cdot \left(-k_l \nabla T_{lattice}\right) = G_{ol}\left(T_{photon} - T_{lattice}\right) \ , \tag{42}$$

where U_e is the electron energy, U_o is the optical photon energy, $T_{electron}$, T_{photon}, $T_{lattice}$ are electron, optical photon, and lattice temperatures. G_{eo} and G_{ol} are the coupling coefficients for the electron-optical phonon and the optical phonon-acoustic phonon, respectively.

4.3 Typical results and further work

Figure 11 shows the evolution of electron density at the surface for a near threshold 100 fs laser pulse from the Feit model [19]. The dashed line shows the pulse intensity profile for multiphoton ionization. This is by far the dominant ionization mechanism,
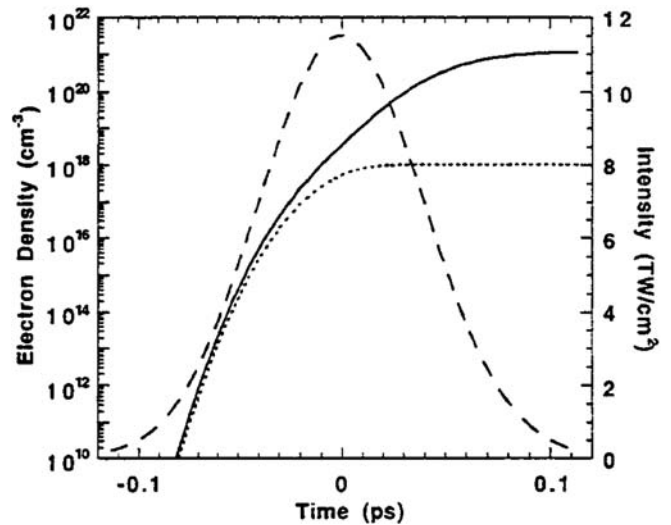

Fig. 11. Production of conduction electrons by multiphoton ionization alone (dotted curve) and by multiphoton plus collisional ionization (solid curve); the incident laser pulse shape is shown by the dashed curve for reference [19]

but drops off rapidly after the peak of the pulse because of the large intensity dependence. After this time, collisional ionization (inverse Bremsstrahlung) results in a short conventional electron avalanche.

According to [20], time and spatial resolved (x direction) electron and lattice temperatures can be calculated. Figure 12 shows the evolution of the surface electron temperature, and the lattice temperature is shown in Fig. 13.

The assumption of local quasiequilibrium is adopted in this model and the particle number density, electron energy, and lattice energy are calculated via the relaxation time approximation to the Boltzmann transport equation. However, given the short pulse duration (0.1 ps), as compared to the electron-lattice relaxation time (0.5 ps), this approximation still has some limitations.
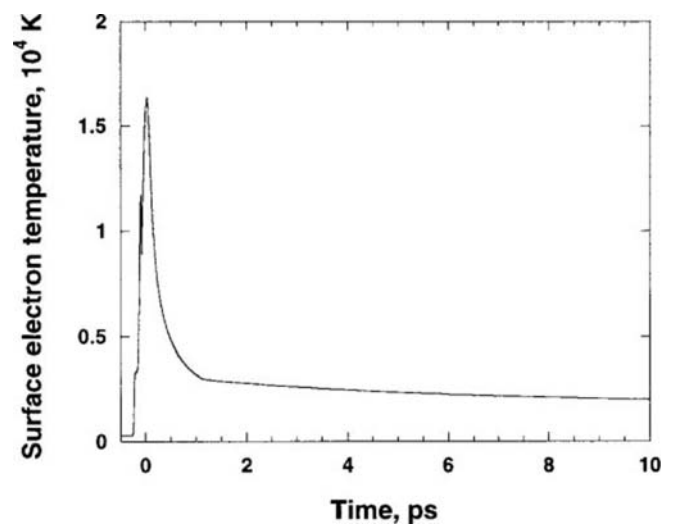

Fig. 12. Evolution of surface electron temperature at $F = 1.5 \, \text{J/cm}^2$ [20]
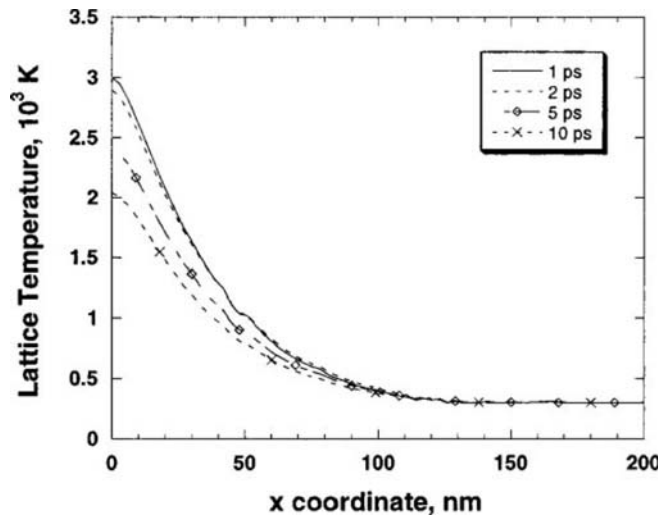
Fig. 13. Lattice temperature at $F = 1.5\,\text{J/cm}^2$ [20]

Many models assume that thermal diffusion is negligible. However, [21] has suggested that there are limits to these claims. At fluences far above the threshold for ablation, thermal effects are observed, including the presence of material that has melted and undergone viscous flow. Moreover, the thermal problems become more complex if the energy delivered is such that the plasma can deliver a significant amount of energy to the surrounding material. So, in the future, new problems such as relaxation time approximation, high laser fluence ablation, and plasma effect on thermal diffusion need to be studied more carefully and quantitative descriptions need to be developed.

5 Conclusions

Laser material interactions exhibit significant differences when the interaction time changes from continuous to an extremely small time scale (femtosecond). In laser cutting using a continuous wave or long-pulsed laser, the primary material removal mechanism melts with molten metal ejected by an assisting oxygen jet. The model developed quantitatively predicts the effects of hydrodynamic instability coupled with oxidation, on the basis of which, striation frequency and depth are predicted and validated. In the future, the calculation of heat transfer and oxidation will be extended to three-dimensional realistic cut geometry, and the effect of vaporization and multiple reflections needs to be considered.

In laser machining using a Q-switched laser with pulse width on the order of nanoseconds, Stefan and kinetic boundary conditions are applied at the liquid-vapor interface, and property discontinuity across the Knudsen layer is considered. Heat conduction is calculated using the enthalpy method. A numerical model is provided to simulate the microscale cavity formation under a high-intensity, pulsed laser irradiation. The complete

thermal interaction between plasma and melted material is still unclear and needs to be studied in the future.

When the laser pulse width further reduces to the order of femtoseconds, as in a Ti:sapphire laser, thermal diffusion can be neglected in most cases due to the ultrashort pulse duration and nonlinear absorption such as miltiphoton ionization and avalanche ionization. These ionization processes need to be considered when modeling the material removal process. More problems need to be considered such as limitation of relaxation time approximation, high laser fluence ablation, and plasma effect on thermal diffusion.

References

1. Powell J (1993) CO$_2$ laser cutting. Springer, Berlin Heidelberg New York
2. Duley W (1996) UV lasers: effects and applications in material science. Cambridge University Press, Cambridge
3. Chichkov BN, Momma C, Nolte S, von Alvensleben F, Tunnermann A (1996) Femtosecond, picosecond, and nanosecond laser ablation of solids. Appl Phys A: Solids Surf 63:109–115
4. MRL Columbia University, NMRC University of Nebraska-Lincoln, RCAM Southern Methodist University (2000) Combined research and curriculum development nontraditional manufacturing (NTM). http://www.mrl.columbia.edu/ntm/index.html. Cited 17 Oct 2000
5. Arata Y, Abe N, Abe E (1979) Dynamic behavior in laser gas cutting of mild steel. Trans JWRI 8(2):15–26
6. Schuocker D (1986) Dynamic phenomena in laser cutting and cut quality. Appl Phys B 40:9–14
7. Ivarson A, Powell J, Kamalu J (1994) The oxidation dynamics of laser cutting of mild steel and the generation of striations on the cut edge. J Mater Process Technol 40:359–374
8. Chen K, Yao YL (1999) Striation formation and melt removal in the laser cutting process. SME J Manuf Process 1(1):43–53
9. Schlichting H (1979) Boundary-layer theory. McGraw-Hill, New York
10. Craik AD (1966) Wind-generated waves in thin liquid films. J Fluid Mech 26:269–392
11. Paek UC, Gagliano FP (1972) Thermal analysis of laser drilling processes. IEEE J Quantum Electron 8:112–119
12. Dabby FW, Paek UC (1972) High-intensity laser-induced vaporization and explosion of solid material. IEEE J Quantum Electron 8(2):106–111
13. Ho JR, Grigoropoulos CP, Humphrey JAC (1995) Computational model for the heat transfer and gas dynamics in the pulsed laser evaporation of metals. J Appl Phys 78(4):4696–4709
14. Zhang W, Yao YL, Chen K (2001) Modeling and analysis of UV laser micromachining of copper. Int J Adv Manuf Technol 18:323–331
15. Bennett TD, Krajnovich DJ, Grigoropoulos CP (1997) Marangoni mechanism in pulsed laser texturing of magnetic disk substrates. J Heat Transf 119:589–596
16. Voller VR, Prakash C (1987) A fixed grid numerical modeling methodology for convection-diffusion mushy region phase-change problems. Int J Heat Mass Transf 30(8):140–145
17. Knight CJ (1979) Theoretical modeling of rapid surface vaporization with back pressure. AIAA J 17(5):519–523
18. Shirk MD, Molian PA (1998) A review of ultrashort pulsed laser ablation of materials. J Laser Appl 10(1):18–28
19. Feit MD, Rubenchik AM, Shore BW (1996) Unique aspects of laser energy deposition in the fs pulse regime. SPIE Proc Ser 2672:243–249
20. Choi TY, Grigoropoulos CP (2002) Plasma and ablation dynamics in ultrafast laser processing of crystalline silicon. J Appl Phys 92(9):4918–4925
21. Luft A, Franz U, Emsermann A, Kaspar J (1996) A study of thermal and mechanical effects on materials induced by pulsed laser drilling. Appl Phys A: Solids Surf 63:93–101